

Stabilizing O3-type layered oxide cathodes through Zn doping for high-energy sodium-ion batteries

Original

Stabilizing O3-type layered oxide cathodes through Zn doping for high-energy sodium-ion batteries / Sperati, V., Darjazi, H., Balducci, L., Langella, A., Massaro, A., Munoz-Garcia, A.B., Pavone, M., Proietti, R.Z., Gerbaldi, C., Elia, G.A.. - In: JOURNAL OF POWER SOURCES. - ISSN 0378-7753. - 687:(2026), pp. 1-10. [10.1016/j.jpowsour.2026.240482]

Availability:

This version is available at: 11583/3011827 since: 2026-06-09T14:57:11Z

Publisher:

Elsevier

Published

DOI:10.1016/j.jpowsour.2026.240482

Terms of use:

This article is made available under terms and conditions as specified in the corresponding bibliographic description in the repository

Publisher copyright

(Article begins on next page)



Stabilizing O3-type layered oxide cathodes through Zn doping for high-energy sodium-ion batteries

Valeria Sperati^{a,b,c}, Hamideh Darjazi^{a,c}, Leonardo Balducci^{a,c}, Aniello Langella^{c,d}, Arianna Massaro^{c,d}, Ana B. Muñoz-García^{c,e}, Michele Pavone^{c,d}, Remo Zaccaria Proietti^b, Claudio Gerbaldi^{a,c,*}, Giuseppe Antonio Elia^{a,c,**}

^a GAME Lab, Department of Applied Science and Technology (DISAT), Politecnico di Torino, Corso Duca degli Abruzzi 24, 10129, Torino, Italy

^b DELTA Lab, Italian Institute of Technology (IIT), Via Morego 30, 16163, Genoa, Italy

^c National Reference Center for Electrochemical Energy Storage (GISEL), INSTM, Via Giusti 9, 50121, Florence, Italy

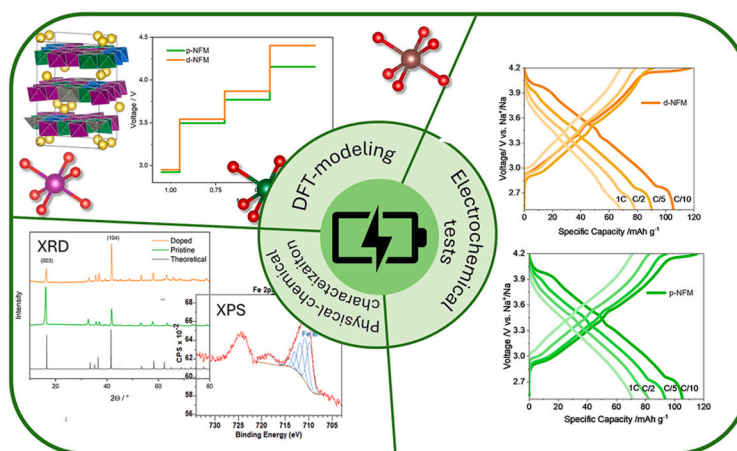
^d Department of Chemical Sciences, University of Naples Federico II, Via Cintia 26, 80126, Naples, Italy

^e Department of Physics "E. Pancini", University of Naples Federico II, Via Cintia 26, 80126, Naples, Italy

HIGHLIGHTS

- Experimental and DFT study of O3-NaNi_{0.33-x}Zn_xFe_{0.17}Mn_{0.5}O₂ (x = 0.0, 0.05).
- Zn-O bonding mitigates transition-metal migration and structural distortion.
- Zn tunes Fe environment by enhancing Fe³⁺/Fe⁴⁺ redox and raising intercalation voltage.
- Zn-doped cathodes show lower polarization, high CE, and stable cycling at 2.0-4.2 V.

GRAPHICAL ABSTRACT



ARTICLE INFO

Keywords:
Sodium battery
Cathode
Layered oxide

ABSTRACT

In this work, we investigate through a combined experimental and computational approach the impact of partially substituting Ni with Zn in O3-type NaNi_{0.33-x}Zn_xFe_{0.17}Mn_{0.5}O₂ (x = 0, 0.05) layered cathodes, a representative high-capacity system for sodium-ion batteries. Owing to its electrochemical inactivity, Zn²⁺ is

This article is part of a special issue entitled: MDB 2025 : Progresses and Challenges published in Journal of Power Sources.

* Corresponding author. GAME Lab, Department of Applied Science and Technology (DISAT), Politecnico di Torino, Corso Duca degli Abruzzi 24, 10129, Torino, Italy.

** Corresponding author. GAME Lab, Department of Applied Science and Technology (DISAT), Politecnico di Torino, Corso Duca degli Abruzzi 24, 10129, Torino, Italy.

E-mail addresses: claudio.gerbaldi@polito.it (C. Gerbaldi), giuseppe.elia@polito.it (G.A. Elia).

<https://doi.org/10.1016/j.jpowsour.2026.240482>

Received 9 January 2026; Received in revised form 5 May 2026; Accepted 20 May 2026

Available online 2 June 2026

0378-7753/© 2026 The Authors. Published by Elsevier B.V. This is an open access article under the CC BY license (<http://creativecommons.org/licenses/by/4.0/>).

incorporated into the layered structure without altering the rhombohedral R-3m symmetry of the as-prepared material. Experimental characterization and first-principles calculations suggest that the presence of Zn–O bonds can contribute to limiting transition-metal migration into the Na layers and to mitigating lattice distortion during Na extraction, thereby supporting a more reversible O3–P3 phase transition. Zn doping improves the local electronic environment of Fe, modulating the $\text{Fe}^{3+}/\text{Fe}^{4+}$ redox activity. Electrochemical measurements confirm that Zn doping reduces electrode polarization and contributes to cycling stability, even within the extended 2.0–4.2 V window where structural degradation is typically severe. These results indicate that Zn substitution is an effective strategy to improve the structural and electrochemical stability of O3-type layered cathodes for advanced NIBs.

1. Introduction

The growing global demand for sustainable and cost-effective energy storage systems has driven intensive research into alternatives to lithium-ion batteries (LIBs). While LIBs dominate the market for portable electronics and electric vehicles, their dependence on scarce and unevenly distributed lithium resources raises challenges for long-term scalability [1,2]. Sodium-ion batteries (Na-ion batteries, NIBs) have therefore emerged as a promising alternative thanks to the abundance, low cost, and wide availability of sodium [3,4]. Moreover, NIBs work on the same “rocking-chair” mechanism as LIBs, in which alkali ions are de-/intercalated in the electrodes during cycling. This similarity provides a strong basis for transferring existing knowledge from LIBs to NIBs in large-scale energy storage applications.

Among the various potential candidates for cathode materials in NIBs, layered transition metal oxides (NaTMO_2 , TM = Mn, Fe, Ni, etc.) are particularly attractive due to their high specific capacity, good structural properties, and compatibility with synthesis methods already established for LIBs [5,6]. Various types of polymorphs exist, differing in the stacking of atoms in the unit cell. In Delmas notation, phases are classified based on sodium coordination environment (P: prismatic and O: octahedral) and the number of distinct oxygen layers [7]. O3-type layered oxides have emerged as promising candidates as NIB cathodes owing to their higher initial Na content and thus enhanced theoretical specific capacity [8], while in comparison, P2 counterparts usually exhibit better rate performance [9,10]. Despite these phase-specific electrochemical features, layered oxides suffer from severe structural instabilities that limit their practical application. During cycling, the crystalline lattice experiences significant structural stress upon repeated sodiation/desodiation, leading to distortions and ultimately irreversible phase transitions. Additionally, these materials are highly sensitive to air and moisture, and their operation at high voltage can trigger oxygen loss [11,12]. Collectively, structural instability, TM migration, and cation mixing can result in accelerated electrode degradation, thus voltage decay and rapid capacity fading upon operation.

Although similar challenges were addressed in LIBs, the larger ionic radius of sodium further reduces structural stability and lowers the theoretical specific capacity [13]. A key priority in designing advanced sodium layered oxide cathodes is to identify strategies that stabilize the layered framework during cycling while preserving electrochemical performance. As the host structure directly determines the achievable capacity, bridging the performance gap between LIBs and NIBs requires identifying materials that combine high redox activity with structural stability. Given that the energy density of NIBs is primarily determined by the cathode, the development of stable, high-capacity, and long-life positive electrodes is a main focus in the field.

In the pursuit of high-energy systems for large-scale and stationary applications, O3-type Fe- and Mn-based layered oxides are promising cathode candidates owing to their abundance, environmental compatibility, and high discharge capacity. However, single-TM systems, such as Na_xFeO_2 and Na_xMnO_2 , face several issues. Na_xFeO_2 undergoes multiple phase transitions during cycling, exhibits poor air stability, and shows limited cycling stability and rate performance [14,15]. These drawbacks are primarily attributed to Fe^{3+} migration into the Na layer during deep

desodiation, where migrated Fe species act as structural pinning centers that hinder reversible slab gliding and lead to partial irreversibility of the phase transition [16]. Na_xMnO_2 is affected by the Jahn–Teller distortion of Mn^{3+} , which localizes electrons and impedes Na^+ diffusion, leading to poor performance and a low specific capacity.

For these reasons, multi-TM systems are extensively studied. Mn-based layered oxides co-substituted with Fe and Ni are particularly promising: Fe enhances redox activity and facilitates Na^+ insertion/extraction, while Ni contributes a two-electron redox process per atom, potentially increasing capacity. Nevertheless, multi-TM systems still face intrinsic structural instabilities that must be mitigated to achieve practical applications. Several approaches have been explored to address these issues, including surface coatings, multiphase design, and cation substitution [17,18]. Among them, metal doping is especially effective in tuning the electronic structure, modulating interlayer spacing, and suppressing irreversible phase transitions [19–24]. For instance, Ti^{4+} substitution enhances structural stability but increases the material cost, while Ca^{2+} incorporation enlarges Na^+ layer spacing and slows Na^+ kinetics due to its larger ionic radius. Achieving tailored composition at the TM site is key to retain the layered framework, ensure efficient Na^+ diffusion, and mitigate voltage decay.

In this context, Zn substitution has attracted significant interest [25–29]. Although Zn^{2+} is electrochemically inactive, its strong electron-donating character can be beneficial in increasing the oxygen electron density, which reduces lattice strain and internal distortion during sodium ion intercalation/deintercalation [30,31]. It has been shown that a suitable amount of Zn incorporation can improve the reversibility of the O3–P3 phase transition [32], mitigate the Mn^{3+} -induced Jahn–Teller distortion [33], limit Fe^{3+} migration into the Na layer [34], and enhance air and moisture stability [35]. However, the majority of studies have been conducted in a limited voltage range (2.0–4.0 V), while irreversible reactions occur almost exclusively above (~4.2 V). With the growing demand for high-energy-density systems, a deeper understanding of the role of Zn doping on the structural stability and redox activity of O3– NaTMO_2 is essential.

In this work, we combine experimental characterization with first-principles calculations to investigate Zn substitution in O3-type $\text{NaNi}_{0.33-x}\text{Zn}_x\text{Fe}_{0.17}\text{Mn}_{0.5}\text{O}_2$ ($x = 0.0, 0.05$). The selection of 5% Zn was based on the need to introduce local structural modulation while minimizing capacity loss due to electrochemically inactive Zn^{2+} . This amount achieves a measurable reduction in lattice distortion without significantly impacting the theoretical capacity, a choice supported by existing literature [25,26,28]. We examine this substitution within both the extended (from 2.0 up to 4.2 V vs. Na^+/Na) and the reduced (2.0–4.0 V) windows. By partially replacing Ni^{2+} with Zn^{2+} , we demonstrate that Zn not only stabilizes the structure and enhances the reversibility of the O3–P3 phase transition, but also modifies the local electronic environment of the TM–O framework and indirectly activates $\text{Fe}^{3+/4+}$ redox processes, as revealed by density functional theory (DFT) calculations.

2. Methods

2.1. Materials preparation

Pristine (undoped) $\text{NaNi}_{0.33}\text{Fe}_{0.17}\text{Mn}_{0.5}\text{O}_2$ (p-NFM) and Zn-doped $\text{NaNi}_{0.28}\text{Zn}_{0.05}\text{Fe}_{0.17}\text{Mn}_{0.5}\text{O}_2$ (d-NFM) materials were synthesized via a solid-state synthesis method using $\text{NaNi}_{0.33-x}\text{Zn}_x\text{Fe}_{0.17}\text{Mn}_{0.5}(\text{OH})_2$ and Na_2CO_3 as precursors [36–38]. The $\text{NaNi}_{0.33-x}\text{Zn}_x\text{Fe}_{0.17}\text{Mn}_{0.5}(\text{OH})_2$ precursor was obtained through a hydroxide co-precipitation, where $\text{NiSO}_4 \cdot 6\text{H}_2\text{O}$ (Merck, 98%), $\text{ZnSO}_4 \cdot 7\text{H}_2\text{O}$ (Merck, 99%), $\text{FeSO}_4 \cdot 7\text{H}_2\text{O}$ (Merck, 97%), and $\text{MnSO}_4 \cdot \text{H}_2\text{O}$ (Merck, Reagent Plus® ≥99%) were dissolved in distilled water in stoichiometric proportions. Then, the obtained precursor and Na_2CO_3 (Na: TM = 1.1:1) were calcined in air at 900 °C for 10 h. The resulting layered oxide powder was stored in an argon-filled glovebox to prevent reactions with moisture.

2.2. Materials characterization

The morphology of the products was characterized using a scanning electron microscope (SEM) operated on a Jeol JSM-6490LA SEM equipped with an energy-dispersive X-ray spectrometer (EDX) to map the sample's composition. The crystal structure was characterized using a powder X-ray diffractometer (XRD, Malvern PANalytical Empyrean) over a scattering angle range of 10°–90° (2θ), with copper Kα radiation as the X-ray source. X-ray photoelectron spectroscopy (XPS), performed on a Kratos Axis Ultra^{DLD} spectrometer (Kratos Analytical Ltd.), was used to analyze the oxidation states of the components. An air stability test was conducted (Fig. S2) to investigate possible phase transitions by morphology analysis using an Empyrean, series III, Malvern Panalytical diffractometer.

2.3. Electrochemical tests

The electrochemical behavior was evaluated using both the three-electrode Swagelok and the coin cell configurations. Cathodes were prepared by mixing active material, carbon black (C-65, Merck), and Kynar® HSV 1810 binder (in a 80:10:10 composition, respectively) in N-methyl-2-pyrrolidone (NMP, Merck), followed by a coating onto aluminum foil substrates. The electrolyte solution consisted of 1 M NaPF_6 in EC:DMC (1:1 v/v), (E-Lyte).

The electrochemical tests, including galvanostatic charge-discharge cycling, cyclic voltammetry (CV), and rate capability, were conducted at ambient laboratory temperature on a VMP3 multichannel electrochemical workstation (BioLogic, France) test system. The voltage range depended on the type of test: 2.5–4.2 V for cycling and rate measurements and 2.0–4.0 V for CV, vs. Na^+/Na .

2.4. Structural models and computational details

Spin-polarized density functional theory (DFT) calculations were performed for the O3-type structure of both pristine ($\text{NaNi}_{0.33}\text{Fe}_{0.17}\text{Mn}_{0.5}\text{O}_2$, p-NFM) and Zn-doped ($\text{NaNi}_{0.25}\text{Zn}_{0.08}\text{Fe}_{0.17}\text{Mn}_{0.5}\text{O}_2$, d-NFM) compositions at various sodium contents ($0.25 \leq x_{\text{Na}} \leq 1.0$) to simulate the cathode charging process [39–42]. Structural models for p-NFM and d-NFM were constructed using $3 \times 2 \times 1$ supercells obtained through orthogonal transformation of the original hexagonal unit cells (space group 166, $R\bar{3}m$), yielding cells containing 117 to 144 atoms. In the fully sodiated configuration, the supercell contains 36 Na atoms and 36 TM atoms distributed across the three slabs (36 f.u., corresponding to 12 atoms per layer and 144 atoms in the whole supercell). The exact number of atoms and their distribution per layer are explicitly reported in Table S1 in the Supporting Information, together with the resulting atomic ratios. The homogeneous Na and TM distributions were implemented via the special quasi-random structure (SQS) approach by means of the SQSgen code [43,44].

Geometry optimization was carried out within the generalized gradient approximation (GGA) using the Perdew-Burke-Ernzerhof (PBE) exchange-correlation functional [45]. To address the self-interaction error commonly encountered in DFT-GGA for localized 3d electrons, the DFT+U scheme was applied with an effective on-site correction parameter ($U-J$)_{eff} = 5.0 eV for the Mn, Ni, and Fe d shells [46,47], and we also added the D3-BJ dispersion correction to account for van der Waals (vdW) interactions [48]. The projector augmented wave (PAW) method was employed as implemented in the Vienna Ab initio simulation package (VASP6.4.2) [49–51], with a plane-wave kinetic energy cutoff of 700 eV and a k-point sampling restricted to the Γ point in reciprocal space. These numerical parameters ensured for our supercell model a total energy convergence within 3 meV per formula unit. The electronic self-consistency convergence thresholds for electronic minimization and ionic forces were set at 10^{-5} eV and 10^{-3} eV Å⁻¹, respectively. Electronic structure was further refined at the HSE06 level of theory [52–54] on the PBE+U minimum-energy structures to achieve higher accuracy, including the Tkatchenko–Scheffler (TS) correction accounting for vdW dispersion forces as implemented in the FHI-aims package [52,55].

3. Results and discussion

3.1. Structural and morphological characterization

The phase and crystal structures of $\text{NaNi}_{0.33}\text{Fe}_{0.17}\text{Mn}_{0.5}\text{O}_2$ (p-NFM) and $\text{NaNi}_{0.28}\text{Zn}_{0.05}\text{Fe}_{0.17}\text{Mn}_{0.5}\text{O}_2$ (d-NFM) powders were characterized by X-ray diffraction (XRD) (Fig. 1a). The diffraction patterns of both samples can be indexed to the O3-type α - NaFeO_2 layered structure with a rhombohedral $R\bar{3}m$ symmetry (space group 166) [56], confirming that the layered framework is preserved upon doping and that Zn^{2+} ions are fully integrated into the host lattice. The O3-type α - NaFeO_2 structure, sketched in Fig. 1b, features transition metal layers stacked in an ABCABC sequence with sodium ions occupying octahedral sites between these layers [57]. Minor impurity peaks related to nickel are present in both samples, as commonly reported for this synthesis route [58].

A closer view of the (003) peak of the O3 phase (inset of Fig. 1a) reveals a shift toward higher angles in d-NFM, indicating a subtle structural change induced by Zn incorporation [59]. Moreover, the (104) peak intensity is higher in d-NFM than p-NFM, with the corresponding decrease in the I_{003}/I_{104} intensity.

Rietveld refinements of the XRD patterns were carried out using the FullProf suite software (Fig. 1c and d), and the results are summarized in Table S2 and S3 in the Supplementary Information. The refined lattice parameters of d-NFM ($a, b = 2.9605(4)$ Å; $c = 16.1601(8)$ Å) are slightly larger than those of p-NFM ($a, b = 2.9501(4)$ Å; $c = 16.1012(4)$ Å). This expansion is consistent with the larger ionic radius of Zn^{2+} (0.74 Å) compared with Ni^{2+} (0.69 Å), and with the longer Zn-O bond length relative to Ni-O, as demonstrated in Fig. S1.

For completeness, an aging study was conducted on both samples (Fig. S2), following two weeks of exposure to air. Both samples can still be indexed as an O3 phase; however, the pristine sample exhibited a notable alteration in the I_{003}/I_{104} peak intensity ratio, which is attributed to the removal of sodium from the structure due to the formation of sodium carbonate, while the doped sample maintained a nearly constant ratio.

The morphological features and the elemental distribution of the samples were analyzed by SEM and EDX, as shown in Fig. 1e and f. Both samples show particle sizes ranging from 1 to 3 μm. However, p-NFM appears to exhibit more pronounced particle agglomeration and the formation of secondary-like particles. In contrast, d-NFM shows a more uniform particle distribution, with a tendency toward reduced agglomeration [60,61]. EDX elemental mapping of p-NFM and d-NFM (Fig. S3) confirms a homogeneous distribution of all transition metal elements. Quantitative EDX analysis indicates that the elemental ratios

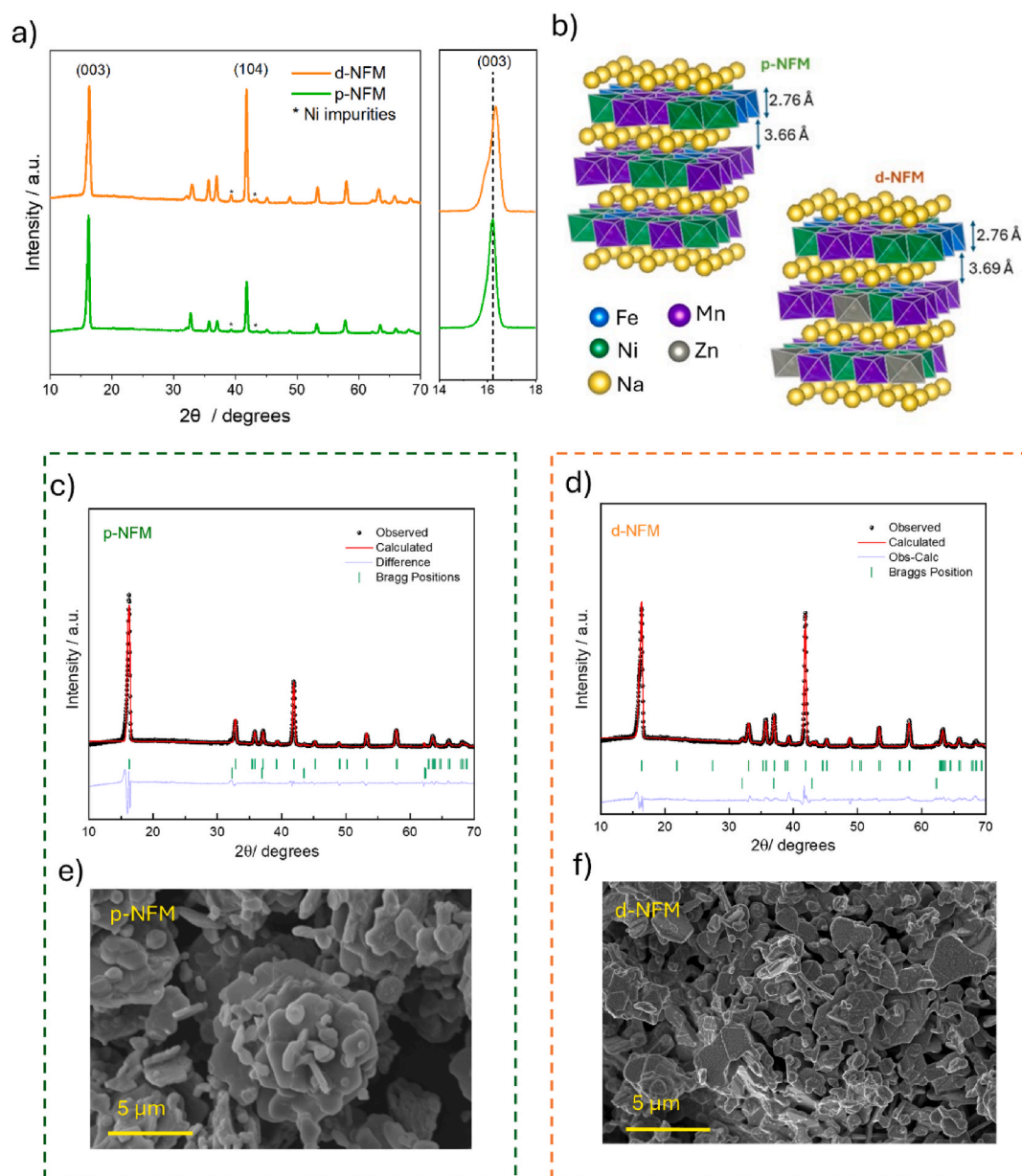


Fig. 1. a) XRD patterns of O3-type layered TM oxides under study: d-NFM (orange) and p-NFM (green), with a box on the righthand side zooming the enlarged (003) reflection. b) Schematic crystal structures of d-NFM and p-NFM, highlighting the interlayer distances between the TM- and Na-layers. Rietveld refinements and SEM images, respectively, of c,e) p-NFM and d,f) d-NFM. (For interpretation of the references to color in this figure legend, the reader is referred to the Web version of this article.)

are consistent with the nominal compositions, as summarized in Table S4.

X-ray photoelectron spectroscopy (XPS) was conducted to investigate the surface chemical states of the samples (Fig. S4 and Fig. 2) [62, 63]. XPS spectra show similar surface compositions for both materials, with characteristic peaks corresponding to the constituent elements (Fig. S4a and b). As shown in Fig. S4e, the Mn 2p peaks [64] appear at binding energies of 642.3 (Mn³⁺) and 644.2 (Mn⁴⁺) eV.

Quantitative fitting of the Mn2p_{3/2} region (Fig. 2a) indicates a Mn³⁺/Mn⁴⁺ ratio of approximately 64%/36% in both materials, suggesting that manganese predominantly exists in the trivalent state. The Ni 2p spectra (Fig. S4f) exhibit two main peaks centered at 854.4 (Ni²⁺) and 856.5 (Ni³⁺) eV. In both samples, Ni²⁺ is the dominant oxidation state (Fig. 2b), although a measurable amount of Ni³⁺ is also present. Notably, d-NFM presents a higher proportion of Ni³⁺ (viz., 19.4 vs. 16.2% for p-NFM), consistent with charge compensation induced by

Mn³⁺ content. The increase in Ni³⁺ content supports the successful incorporation of Zn²⁺ into the TM layer (Ni²⁺). Since Zn typically stabilizes in the +2 oxidation state (due to its filled 3d orbital), electronic charge redistribution among the other transition metals is required to maintain charge neutrality.

The Fe 2p spectra (Fig. S4g and Fig. 2c) show the peaks at 710.8 (Fe³⁺) and 713.0 (Fe⁴⁺) eV, with no significant shift or variation between the two samples, suggesting that Zn substitution does not affect the iron oxidation states during the synthesis route. The Na 1s signal is clearly observed (Fig. S4d), while the Zn²⁺ peak is detected exclusively in the d-NFM sample (Fig. S4c and h) [25,65]. Quantitative XPS analysis provides elemental ratios consistent with the expected stoichiometries (Table S5).

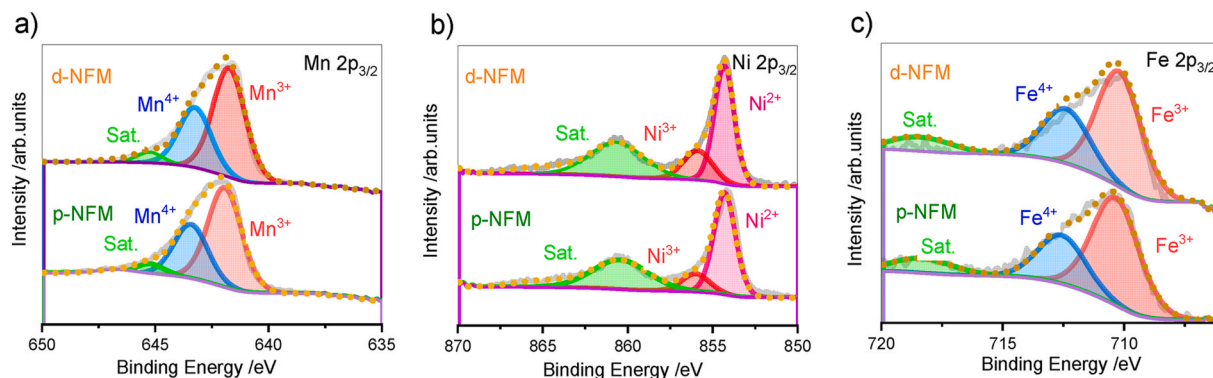


Fig. 2. XPS spectra of a) Mn $2p_{3/2}$, b) Ni $2p_{3/2}$, c) Fe $2p_{3/2}$ regions for p-NFM (lower profiles) and d-NFM (upper profiles) samples. The fitted peaks correspond to different oxidation states ($\text{Mn}^{3+}/\text{Mn}^{4+}$, $\text{Ni}^{2+}/\text{Ni}^{3+}$, $\text{Fe}^{3+}/\text{Fe}^{4+}$), along with associated satellite contributions.

3.2. Computational analysis

Structural evolution of p-NFM and d-NFM upon desodiation was investigated by analyzing the variation of lattice parameters as a function of Na content in the $\text{O}3\text{-Na}_x\text{TMO}_2$ ($x = 1, 0.75, 0.50$, and 0.25 , TM = Ni, Fe, Mn, Zn) models. The minimum-energy structures obtained at PBE+U(-D3BJ) level of theory are shown in Fig. 3a–b, while Table S6 shows the good agreement of theoretical lattice parameters with experimental data, with a limited deviation of $\sim 1\%$ [66].

The theoretical capacity-voltage profile is plotted in Fig. 3c as the sodium intercalation potential derived from Eq. (1):

$$V = \frac{E_{(\text{Na}_{x_2}\text{NFMO})} - E_{(\text{Na}_{x_1}\text{NFMO})} - (x_2 - x_1)\frac{1}{2}E_{\text{Na}}}{(x_2 - x_1)} \quad (\text{Eq. 1})$$

where $E_{(\text{Na}_{x_2}\text{NFMO})}$ and $E_{(\text{Na}_{x_1}\text{NFMO})}$ are the total energies of the samples at sodium contents x_2 and x_1 (with $x_1 < x_2$), and E_{Na} is the total energy of sodium metal considering the bcc lattice with two atoms in the unit cell [67,68]. This method, widely employed to predict cathode behavior during charging, reflects the energy required to extract sodium ions from the host lattice [69–71]. The higher intercalation potential of d-NFM compared to p-NFM (orange and green lines in Fig. 3c, respectively) suggests that electrochemically inactive Zn promotes higher oxidation states of the remaining transition metals. To assess this correlation, we

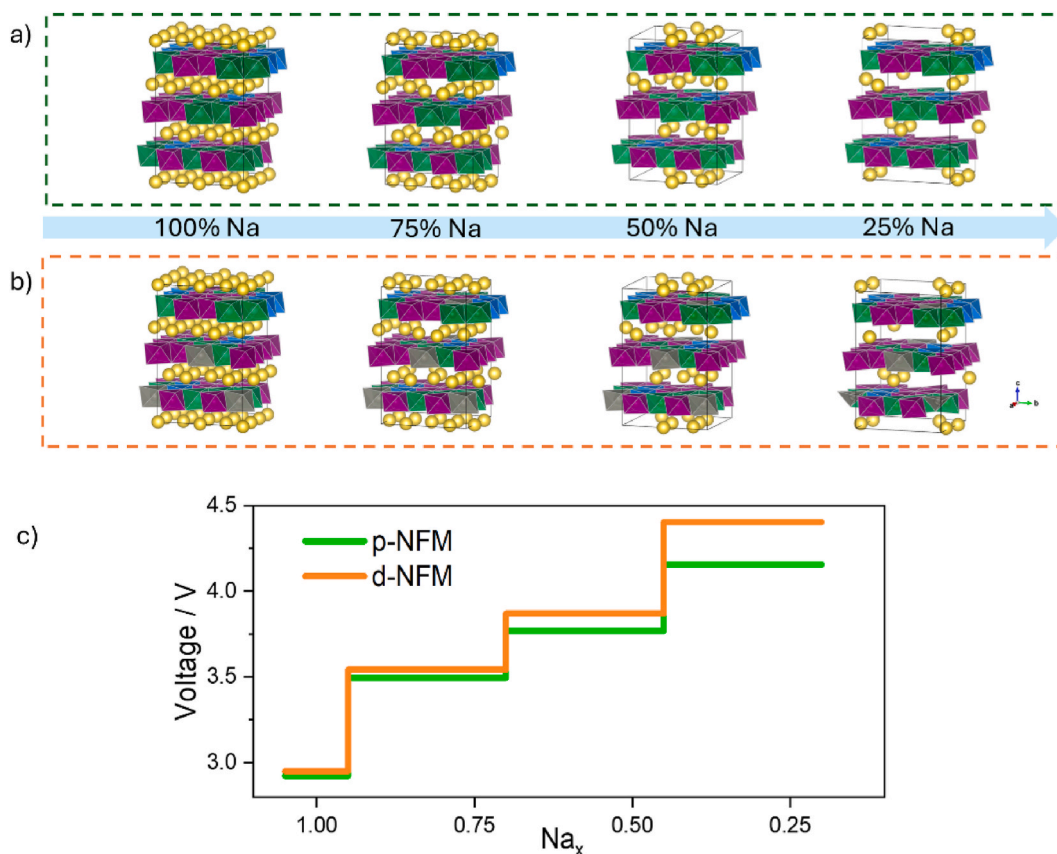


Fig. 3. Structural evolution of the crystalline lattice during desodiation: PBE + U(-D3BJ) minimum-energy structures of a) p-NFM and b) d-NFM at different Na contents. c) Calculated Na intercalation potentials for both materials. Color code: Na (yellow), Ni (green), Mn (violet), Fe (blue), Zn (gray). (For interpretation of the references to color in this figure legend, the reader is referred to the Web version of this article.)

analyzed atomic charges and net magnetizations during charging, *i.e.*, upon sodium removal (same calculations at the DFT+U level of theory are reported in SI Fig.S5). As shown in Fig. 4a–b, the Mn sublattice (violet line, upper panel) is slightly oxidized upon charge, as evidenced by a decrease in average magnetization from 3.27 to 2.99 μ_B in p-NFM and from 3.29 to 2.99 μ_B in d-NFM. This change indicates a small contribution to charge compensation and thus confirms that it mainly plays a structural stabilizer role. Further evidence of this behavior is provided in Fig. S6, which shows the oxidation of Mn from a mixed Mn^{3+}/Mn^{4+} state to a fully Mn^{4+} state occurring early in the deintercalation process. Nickel (light green line) undergoes a progressive $Ni^{2+} \rightarrow Ni^{3+} \rightarrow Ni^{4+}$ oxidation in both pristine and doped materials, with decreasing magnetization indicating the transition from d^8 , d^7 , and then d^6 electronic configurations (*i.e.*, 1.71 \rightarrow 1.19 \rightarrow 0.33 μ_B in p-NFM and 1.54 \rightarrow 0.87 \rightarrow 0.08 μ_B in d-NFM). In contrast, Fe (blue line) remains mainly Fe^{3+} in p-NFM (\sim 4.20 μ_B , d^5 high-spin), while a sizeable amount of Fe^{3+} is oxidized up to Fe^{4+} in d-NFM at low Na content (\sim 3.93 μ_B , at $x = 0.25$). These results highlight the indirect effect of Zn doping in enhancing Fe redox activity at high voltages. To provide a clearer depiction of the oxidation state evolution of each transition metal during desodiation, Fig. S6 illustrates the magnetization of each TM during desodiation. This detailed view provides a clearer representation of changes in oxidation states that are not immediately discernible from the average magnetization.

The charge analysis (Fig. 4c–d, same color code) provides less pronounced trends, consistent with negative-feedback charge regulation (Fig. S7) [72]. Upon desodiation, the Bader charges of the TMs increase progressively, although more smoothly than the corresponding magnetic moments, reflecting partial charge delocalization within the TM–O framework rather than purely ionic oxidation. The absolute magnitude of the oxygen magnetization reflects the degree of TM–O hybridization and is consistent with a cooperative charge-redistribution mechanism within the TM–O framework, without evidence of localized oxygen

oxidation or dimerization. Overall, these results indicate that charge compensation remains dominated by TM oxidation, while oxygen contributes indirectly through increased TM–O covalency. The calculated charge values are far from the ionic limit owing to the highly covalent character of TM–O bonds. The covalent character is also reflected in the angular-momentum projected density of states (pDOS Figs. S8–S9), which shows significant hybridization between TM *d*- and O *p*-states. The overall pDOS profiles of both samples are similar upon desodiation. However, a key difference appears in the electronic behavior of iron at high voltages (and consequently low values of sodium $x = 0.5$ and 0.25). Specifically, Fe *d* bands cross the Fermi level, indicating a change in oxidation state from Fe^{3+} (high-spin d^5 configuration, fully occupied valence band) to Fe^{4+} (d^4 , with unoccupied states in the conduction band). The main difference between the two samples lies in the degree of this partial oxidation, which is more pronounced in the Zn-doped material. These observations are consistent with the magnetization data (Fig. S6) and further supported by the CV results discussed in the following Section 3.3.

Pair distribution functions (PDFs, Figs. S10–12) of TM–O distances calculated for each sodiation degree illustrate the evolution of bond lengths within the TM-centered octahedra during desodiation. Comparative analysis of PDFs reveals whether the TM–O bonds undergo compression as a result of progressive oxidation of the TM centers. As shown in Fig. S9, Ni–O bonds are gradually shortened as sodium content decreases, with the most intense peak shifting from \sim 2.1 to 1.9 Å going from $x_{Na} = 1.0$ to 0.50, consistent with $Ni^{2+} \rightarrow Ni^{3+} \rightarrow Ni^{4+}$ oxidation [68, 70]. Such structural distortions can also be associated to Jahn-Teller (JT) effects in some TM species. For instance, the Mn–O PDFs (Fig. S11) show the characteristic JT distortions of Mn^{3+} , with two distinct peaks at \sim 1.9 and \sim 2.2 Å. Upon desodiation at $x_{Na} = 0.50$, these peaks converge to \sim 1.9 Å, reflecting the stabilizing effect of Mn sublattice. In contrast, the Fe–O bond lengths (Fig. S12) exhibit a broad distribution between 1.9 and 2.2 Å without a distinct peak shift. The

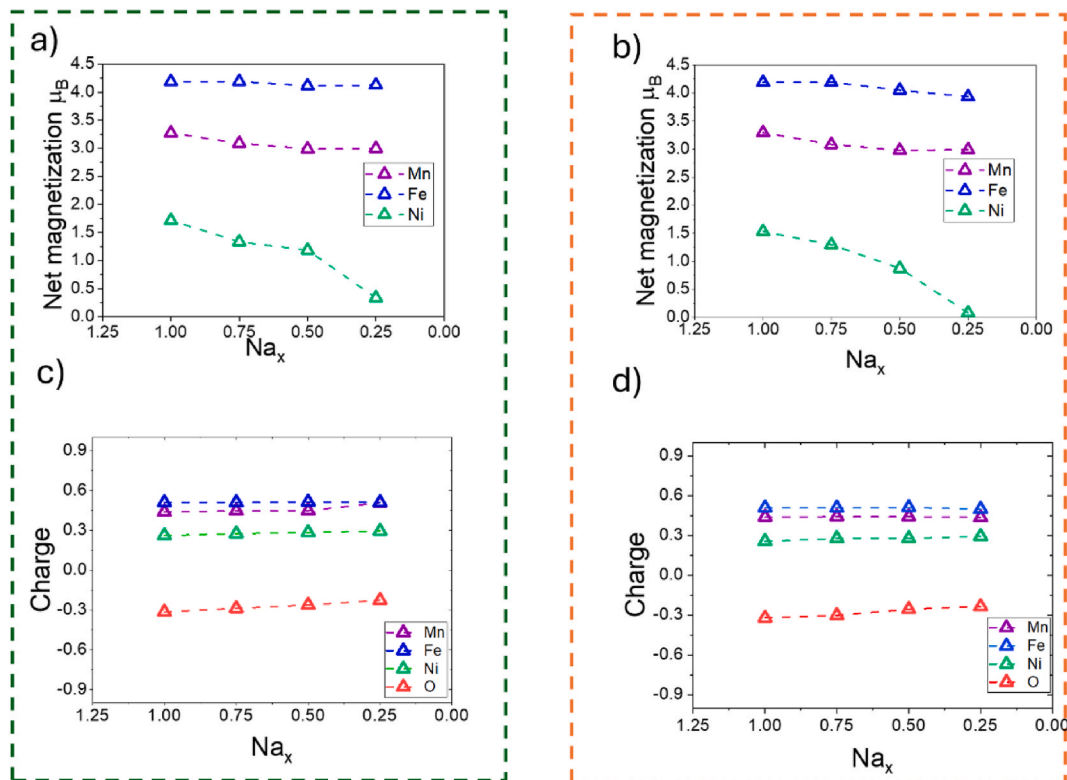


Fig. 4. Electronic structure analysis obtained at HSE06+TS level of theory: a, b) Net magnetization and c, d) Average Bader charges of (left) pristine (p-NFM) and (right) doped (d-NFM) materials for each element: Mn (violet), Fe (blue), Ni (green), and O (red) as a function of Na content. (For interpretation of the references to color in this figure legend, the reader is referred to the Web version of this article.)

absence of a distinct peak shift suggests that oxidation of Fe^{3+} to Fe^{4+} does not significantly shorten the Fe–O bonds, which contrasts with Ni–O bonds that clearly shorten upon Ni oxidation. These results imply that iron is less influenced by electrostatic forces upon oxidation, and FeO_6 octahedra remain largely undistorted [73,74].

3.3. Electrochemical behavior

To complement and validate the insights provided by DFT calculations, particularly the enhanced iron activity in d-NFM, cyclic voltammetry (CV) measurements were performed (Fig. S13a–b). Both samples exhibit a pair of redox peaks at about 2.0–2.3 V vs. Na^+/Na , corresponding to the $\text{Mn}^{3+}/\text{Mn}^{4+}$ redox couple [75], followed by $\text{Ni}^{2+}/\text{Ni}^{3+}$ peaks at 2.5–3.0 V [76], and $\text{Na}^+/\text{vacancy}$ ordering peaks at 3.4–3.5 V [73,77]. In O3-type Na layered oxides, the redox processes in the ~3.6–3.8 V region are widely reported and are commonly associated with the participation of the $\text{Fe}^{3+}/\text{Fe}^{4+}$ redox couple [28,74,78,79], often overlapping with Ni redox activity, depending on the specific composition. Although CV does not directly quantify Fe oxidation-state evolution, which would likely require advanced spectroscopic analysis, the enhanced intensity of this high-voltage feature in the Zn-substituted sample supports the hypothesis of increased Fe participation in charge

compensation. This assignment is reinforced by DFT results, which show a more substantial depopulation of Fe 3d states and a greater reduction in Fe magnetic moments upon desodiation in d-NFM compared to p-NFM. These trends indicate that the presence of zinc enhances the oxidation of the transition metal, in line with the computational findings discussed above. The potential difference between the $\text{Ni}^{2+}/\text{Ni}^{3+}$ redox peaks provides insights into the electrochemical reversibility and polarization behavior of electrode materials. For p-NFM, the large separation (~0.7 V) between the cathodic and anodic peaks associated with Ni indicates pronounced polarization, whereas d-NFM exhibits a much narrower gap (~0.17 V), suggesting reduced polarization and enhanced reversibility. These observations confirm that Zn^{2+} substitution effectively lowers polarization, improves redox reversibility, and enhances stability [80]. The stabilizing effect is likely attributed to the pillar-like role of Zn within the structure, which helps mitigate irreversible distortion and collapse during Na^+ intercalation and deintercalation processes.

The reversible Na^+ ion storage behavior of p-NFM and d-NFM cathodes was evaluated by galvanostatic charge/discharge (GCD) cycling at ambient temperature within 2.5–4.2 V vs. Na^+/Na and at different C-rates (Fig. 5a and b) [81]. Fig. 5a, b displays the GCD voltage vs. specific capacity profiles at rates ranging from C/10 to 1C. Both

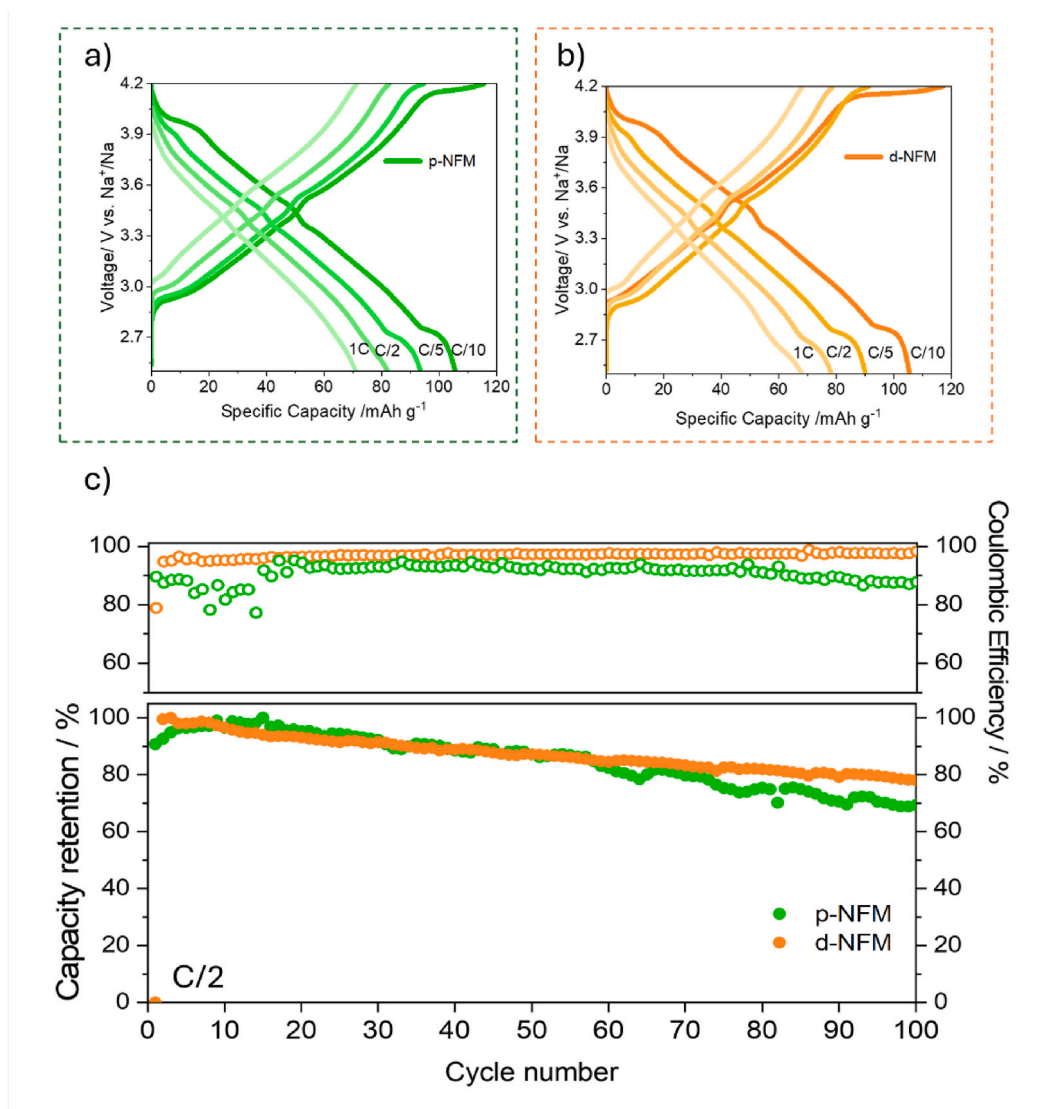


Fig. 5. Representative voltage vs. specific capacity profiles of: a) p-NFM and b) d-NFM resulting from ambient temperature galvanostatic charge/discharge cycling at different C-rates. c) Capacity retention (%) upon long-term cycling performance and coulombic efficiency at C/2 for both materials.

electrodes exhibit characteristic voltage features: during discharge, an initial plateau around 4 V vs. Na⁺/Na corresponds to the O3 to O'3 distortion, followed by a sloping region down to ~2.7 V, and a lower-voltage plateau associated with the O3-P3 transition [82]. Multiple intermediate plateaus between 2.8 and 4.1 V arise from Na⁺/vacancy ordering and related structural rearrangements. During charge, a plateau at ~4.1 V reflects the P3-O''3 transition [83]. Both electrodes demonstrate good electrochemical performance, delivering specific capacities of around 105 and 70 mAh g⁻¹ at C/10 and 1C rates, respectively.

As shown in Fig. 5c, the Zn-doped NFM sample exhibits enhanced electrochemical performance upon long-term cycling compared to pristine NFM. Indeed, it delivers improved capacity retention after 100 cycles, but particularly higher Coulombic efficiency (98.5 vs. 95.9% for d-NFM and p-NFM, respectively), and the improved Coulombic efficiency reflects more reversible phase transitions, facilitated by Zn doping (Fig. S14), which is also reflected in the voltage vs. specific capacity profiles (Fig. 5a and b), where the doped electrode maintains a more consistent characteristic shape upon cycling at higher C-rates. Additionally, the enhanced capacity retention highlights the role of Zn in promoting structural stability during prolonged operation in laboratory scale electrochemical cells vs. Na metal.

4. Conclusion

In conclusion, the current research provides, for the first time, a combined experimental and computational evaluation of the effect of Zn doping in NaNi_{0.28}Zn_{0.05}Fe_{0.17}Mn_{0.5}O₂, offering insights into its structural and electrochemical impact on the O3-type layered oxide. Unlike previous reports, where Zn substitution was primarily considered in other NaTMO₂ compositions for structural stabilization, our study discusses its role in this specific system by correlating experimental observations with DFT analysis. Overall, the slightly improved performance of the Zn-doped material compared to the pristine material can be attributed to multiple factors related to Zn-substitution: (i) stabilization of the structure by non-participation in the redox process; (ii) stabilization of the TM layer by limiting cation migration during deep desodiation; (iii) subtle tuning of the local crystal structure and inter-layer environment, which helps preserve favorable Na⁺ diffusion pathways; (iv) reduced particle agglomeration together with improved elemental homogeneity. The doped d-NFM material maintained the rhombohedral $R\bar{3}m$ structure and a tendency toward reduced particle agglomeration, maintaining good elemental homogeneity. Although Zn itself is electrochemically inactive, DFT calculations have highlighted its significant role in modulating the electronic structure and redox properties, leading to increased intercalation voltages. Electrochemical measurements further confirmed reduced polarization and improved Coulombic efficiency, resulting in stable cycling of the Zn-doped cathode in a laboratory-scale cell vs. Na metal anode. These results establish Zn substitution as a promising approach for tuning the structural and electrochemical properties of O3-type NaTMO₂ cathodes, providing a valuable benchmark for the development of high-performance sodium-ion batteries.

CRedit authorship contribution statement

Valeria Sperati: Conceptualization, Data curation, Writing – original draft. **Hamideh Darjazi:** Conceptualization, Data curation, Supervision, Writing – review & editing. **Leonardo Balducci:** Investigation, Writing – review & editing. **Aniello Langella:** Conceptualization, Investigation, Writing – review & editing. **Arianna Massaro:** Data curation, Supervision, Writing – review & editing. **Ana B. Muñoz-García:** Conceptualization, Supervision, Writing – review & editing. **Michele Pavone:** Conceptualization, Supervision, Writing – review & editing. **Remo Zaccaria Proietti:** Conceptualization, Supervision,

Writing – review & editing. **Claudio Gerbaldi:** Conceptualization, Supervision, Writing – review & editing. **Giuseppe Antonio Elia:** Conceptualization, Supervision, Writing – review & editing.

Declaration of competing interest

The authors declare that they have no known competing financial interests or personal relationships that could have appeared to influence the work reported in this paper.

Acknowledgments

This study was carried out under the National Recovery and Resilience Plan (NRRP), within the NEST – Network 4 Energy Sustainable Transition (Mission 4, Component 2, Investment 1.3 – D.D. 1561 11.10.2022 of the Ministero dell'Università e della Ricerca (MUR), PE0000021), and the MOST – Sustainable Mobility Center and received funding from the European Union Next-GenerationEU (PIANO NAZIONALE DI RIPRESA E RESILIENZA – PNRR eMission 4, Component 2, Investment 1.4 and D.D. 1033 17/06/2022 of the Ministero dell'Università e della Ricerca (MUR), CN00000023). This study was also carried out within the GENESIS project, funded by the Ministero dell'Università e della Ricerca within the PRIN 2022 program (D.D.104 -02/02/2022). This manuscript reflects only the authors' views and opinions, neither the European Union nor the European Commission can be considered responsible for them. Support under the MUR program “Dipartimenti di Eccellenza 2023–2027” (CUPE17G22001490006) is gratefully acknowledged.

Appendix A. Supplementary data

Supplementary data to this article can be found online at <https://doi.org/10.1016/j.jpowsour.2026.240482>.

Data availability

Data will be made available on request.

References

- [1] M.H. Han, E. Gonzalo, G. Singh, T. Rojo, A comprehensive review of sodium layered oxides: powerful cathodes for Na-ion batteries, *Energy Environ. Sci.* 8 (2015) 81–102, <https://doi.org/10.1039/c4ee03192j>.
- [2] C. Zhao, Q. Wang, Z. Yao, J. Wang, B. Sánchez-Lengeling, F. Ding, Y.S. Hu, Rational design of layered oxide materials for sodium-ion batteries, *Science* 370 (6517) (2020) 708–711, <https://doi.org/10.1126/science.aay9972>.
- [3] A. Rudola, R. Sayers, C.J. Wright, J. Barker, Opportunities for moderate-range electric vehicles using sustainable sodium-ion batteries, *Nat. Energy* 8 (2023) 215–218, <https://doi.org/10.1038/s41560-023-01215-w>.
- [4] B. Dunn, H. Kamath, J.M. Tarascon, Electrical energy storage for the grid: a battery of choices, *Science* 334 (6058) (2011) 928–935, <https://doi.org/10.1126/science.1212741>.
- [5] Y.J. Guo, R.X. Jin, M. Fan, W.P. Wang, S. Xin, L.J. Wan, Y.G. Guo, Sodium layered oxide cathodes: properties, practicality and prospects, *Chem. Soc. Rev.* 53 (2024) 7828–7874, <https://doi.org/10.1039/d4cs00415a>.
- [6] L.Y. Kong, H.X. Liu, Y.F. Zhu, J.Y. Li, Y. Su, H.W. Li, H.Y. Hu, Y.F. Liu, M.J. Yang, Z. C. Jian, X.B. Jia, S.L. Chou, Y. Xiao, Layered oxide cathodes for sodium-ion batteries: microstructure design, local chemistry and structural unit, *Sci. China Chem.* 67 (2024) 191–213, <https://doi.org/10.1007/s11426-022-1550-2>.
- [7] C. Delmas, C. Fouassier, P. Hagemuller, Structural classification and properties of the layered oxides, *Physica B+C* 99 (1–4) (1980) 81–85, [https://doi.org/10.1016/0378-4363\(80\)90214-4](https://doi.org/10.1016/0378-4363(80)90214-4).
- [8] Q. Wang, D. Zhou, C. Zhao, J. Wang, H. Guo, L. Wang, Z. Yao, D. Wong, G. Schuck, X. Bai, J. Lu, M. Wagemaker, Fast-charge high-voltage layered cathodes for sodium-ion batteries, *Nat. Sustain.* 7 (2024) 338–347, <https://doi.org/10.1038/s41893-024-01266-1>.
- [9] M. Gao, H. Li, Z. Zhao, X. Wang, Inducing Na⁺ site rearrangement through a cosubstitution strategy for rapid Na diffusion kinetics of P2-Type layered metal oxides, *ACS Appl. Mater. Interfaces* 16 (2024) 14789–14798, <https://doi.org/10.1021/acsmi.3c18341>.
- [10] X. Qi, L. Liu, N. Song, F. Gao, K. Yang, Y. Lu, H. Yang, Y.S. Hu, Z.H. Cheng, L. Chen, Design and comparative study of O3/P2 hybrid structures for room temperature sodium-ion batteries, *ACS Appl. Mater. Interfaces* 9 (2017) 40215–40223, <https://doi.org/10.1021/acsmi.7b11282>.

- [11] J. Wang, Y.F. Zhu, Y. Su, J.X. Guo, S. Chen, H.K. Liu, S.X. Dou, S.L. Chou, Y. Xiao, Routes to high-performance layered oxide cathodes for sodium-ion batteries, *Chem. Soc. Rev.* 53 (2024) 4230–4301, <https://doi.org/10.1039/d3cs00929g>.
- [12] Y.J. Guo, R.X. Jin, M. Fan, W.P. Wang, S. Xin, L.J. Wan, Y.G. Guo, Sodium layered oxide cathodes: properties, practicality and prospects, *Chem. Soc. Rev.* 53 (2024) 7828–7874, <https://doi.org/10.1039/d4cs00415a>.
- [13] N. Yabuuchi, K. Kubota, M. Dahbi, S. Komaba, Research development on sodium-ion batteries, *Chem. Rev.* 114 (2014) 11636–11682, <https://doi.org/10.1021/cr500192f>.
- [14] K. Kubota, T. Asari, H. Yoshida, N. Yaabuuchi, H. Shiiba, M. Nakayama, S. Komaba, Understanding the structural evolution and redox mechanism of a NaFeO₂-NaCoO₂ solid solution for sodium-ion batteries, *Adv. Funct. Mater.* 26 (2016) 6047–6059, <https://doi.org/10.1002/adfm.201601292>.
- [15] N. Yabuuchi, H. Yoshida, S. Komaba, Crystal structures and electrode performance of alpha-NaFeO₂ for rechargeable sodium batteries, *Electrochemistry* 80 (2012) 716–719, <https://doi.org/10.5796/electrochemistry.80.716>.
- [16] S. Chu, C. Zhang, H. Xu, S. Guo, P. Wang, H. Zhou, Pinning effect enhanced structural stability toward a zero-strain layered cathode for sodium-ion batteries, *Angew. Chem., Int. Ed.* 60 (2021) 13366–13371, <https://doi.org/10.1002/anie.202100917>.
- [17] X. Chen, C. Wang, Y. Wang, Y. Zhao, X. Yin, N. Zhang, Recent progress in layered oxide cathodes for sodium-ion batteries: stability, phase transition and solutions, *J. Mater. Chem. A Mater.* (2024), <https://doi.org/10.1039/d4ta03372h>.
- [18] S. Zhao, Q. Shi, W. Feng, Y. Liu, X. Yang, X. Zou, X. Lu, Y. Zhao, Research progress in O3-type Ni/Fe/Mn based layered cathode materials for sodium ion batteries, *Carbon Neutrality* 2 (2023), <https://doi.org/10.1007/s43979-023-00053-9>.
- [19] E. Grépin, Y. Zhou, B. Li, G. Rousse, J.M. Tarascon, S. Mariyappan, Optimal Ti-Substitution in layered oxide cathodes for Na-Ion batteries, *Chem. Mater.* (2024), <https://doi.org/10.1021/acs.chemmater.4c02501>.
- [20] X. Xia, T. Liu, C. Cheng, H. Li, T. Yan, H. Hu, Y. Shen, H. Ju, T.S. Chan, Z. Wu, Y. Su, Y. Zhao, D. Cao, L. Zhang, Suppressing the dynamic oxygen evolution of sodium layered cathodes through synergistic surface dielectric polarization and bulk site-selective Co-Doping, *Adv. Mater.* 35 (2023), <https://doi.org/10.1002/adma.202209556>.
- [21] Q. Wang, S. Mariyappan, J. Vergnet, A.M. Abakumov, G. Rousse, F. Rabuel, M. Chakir, J.M. Tarascon, Reaching the energy density limit of layered O3-NaNi_{0.5}Mn_{0.5}O₂ electrodes via dual Cu and Ti substitution, *Adv. Energy Mater.* 9 (2019), <https://doi.org/10.1002/aenm.201901785>.
- [22] J. Feng, S. hua Luo, Y.X. Dou, J. Cong, X. Liu, P. Li, S. Yan, Q. Wang, Y. Zhang, X. Lei, J. Gao, Facile design and synthesis of Co-free layered O3-type NaNi_{0.2}Mn_{0.2}Fe_{0.6}O₂ as promising cathode material for sodium-ion batteries, *J. Electroanal. Chem.* 914 (2022), <https://doi.org/10.1016/j.jelechem.2022.116301>.
- [23] X. Li, X. Shen, J. Zhao, Y. Yang, Q. Zhang, F. Ding, M. Han, C. Xu, C. Yang, H. Liu, Y.S. Hu, O3-NaFe(1/3-x)Ni_{1/3}Mn_{1/3}Al_xO₂ Cathodes with improved air stability for Na-Ion batteries, *ACS Appl. Mater. Interfaces* 13 (2021) 33015–33023, <https://doi.org/10.1021/acsami.1c07554>.
- [24] Ş. Patat, A. Şahin, Y. Taş, F. Şanlı, Y. Yılmaz, T. Öztürk, A novel air-stable O3-type layered oxide cathode material with low Ni content for sodium-ion batteries, *Int. J. Energy Res.* 46 (2022) 22025–22037, <https://doi.org/10.1002/er.8230>.
- [25] Q. Mao, C. Zhang, W. Yang, J. Yang, L. Sun, Y. Hao, X. Liu, Mitigating the voltage fading and lattice cell variations of O3-NaNi_{0.2}Fe_{0.35}Mn_{0.45}O₂ for high performance Na-ion battery cathode by Zn doping, *J. Alloys Compd.* 794 (2019) 509–517, <https://doi.org/10.1016/j.jallcom.2019.04.271>.
- [26] S. Mariyappan, T. Marchandier, F. Rabuel, A. Iadecola, G. Rousse, A.V. Morozov, A. M. Abakumov, J.M. Tarascon, The role of divalent (Zn²⁺/Mg²⁺/Cu²⁺) substituents in achieving full capacity of sodium layered oxides for Na-Ion battery applications, *Chem. Mater.* 32 (2020) 1657–1666, <https://doi.org/10.1021/acs.chemmater.9b05205>.
- [27] T. Zhang, M. Ren, Y. Huang, F. Li, W. Hua, S. Indris, F. Li, Negative lattice expansion in an O3-Type transition-metal oxide cathode for highly stable sodium-ion batteries, *Angew. Chem., Int. Ed.* 63 (2024), <https://doi.org/10.1002/anie.202316949>.
- [28] P. Liu, T. Zhan, X. Chen, H. Li, Q. Wang, W. Lu, L. Jiao, Regulating phase stability of O3-Type-Layered oxide cathode via Zn²⁺ substitution, *J. Phys. Chem. C* 127 (2023) 20632–20639, <https://doi.org/10.1021/acs.jpcc.3c05873>.
- [29] D. Chen, B. He, S. Jiang, X. Wang, J. Song, H. Chen, D. Xiao, Q. Zhao, Y. Meng, Y. Wang, Enhancing the structural stability and strength of P2-type layered oxide sodium ion battery cathodes by Zn/F dual-site doping, *Chem. Eng. J.* 510 (2025), <https://doi.org/10.1016/j.cej.2025.161676>.
- [30] X. Wu, G.L. Xu, G. Zhong, Z. Gong, M.J. McDonald, S. Zheng, R. Fu, Z. Chen, K. Amine, Y. Yang, Insights into the effects of zinc doping on structural phase transition of P2-Type sodium nickel manganese oxide cathodes for high-energy sodium ion batteries, *ACS Appl. Mater. Interfaces* 8 (2016) 22227–22237, <https://doi.org/10.1021/acsami.6b06701>.
- [31] Y. Sun, P. Zhou, S. Liu, Z. Zhao, Y. Pan, X. Shen, X. Wu, J. Zhao, J. Wang, J. Zhou, Manipulating Na occupation and constructing protective film of P2-Na_{0.67}Ni_{0.33}Mn_{0.67}O₂ as long-term cycle stability cathode for sodium-ion batteries, *J. Energy Chem.* 88 (2024) 603–611, <https://doi.org/10.1016/j.jechem.2023.09.042>.
- [32] W. Qin, Y. Liu, J. Liu, Z. Yang, Q. Liu, Boosting the ionic transport and structural stability of Zn-doped O3-type NaNi_{1/3}Mn_{1/3}Fe_{1/3}O₂ cathode material for half/full sodium-ion batteries, *Electrochim. Acta* 518 (2022), <https://doi.org/10.1016/j.jelectacta.2022.140357>.
- [33] M. Li, L. Chen, Z. Liu, L. Tang, D.A. Podgorny, H. Xian, X. Niu, R. Wu, J.S. Chen, Lattice stabilization in P2-Type layered oxide cathodes by Zn doping for high-voltage sodium storage, *ACS Appl. Mater. Interfaces* 17 (2025) 49630–49638, <https://doi.org/10.1021/acsaami.5c13407>.
- [34] R. Liu, S. Yang, S. Zhou, J. Xing, X. Niu, G. Pang, G. Liu, F. Ye, B. Xiao, C. Xu, Regulating reversible phase transition at high voltage window on O3-Type layered cathodes by doping Zn for sodium-ion batteries, *Small* (2025), <https://doi.org/10.1002/sml.202505197>.
- [35] Y. Cai, Z. Luo, K. Liao, X. Xin, M. Zhou, Y.J. Cheng, R. Liu, X. Yan, S. Papović, K. Zheng, K. Świerczek, Dual-site Zn doping boosts longevity and air stability of O3-type NaNi_{1/3}Fe_{1/3}Mn_{1/3}O₂ cathode for high-performance sodium-ion batteries, *J. Power Sources* 631 (2025), <https://doi.org/10.1016/j.jpowsour.2025.236272>.
- [36] J.H. Mugumya, M.L. Rasche, R.F. Rafferty, A. Patel, S. Mallick, M. Mou, J.A. Bobb, R.B. Gupta, M. Jiang, Synthesis and theoretical modeling of suitable Co-precipitation conditions for producing NMC111 cathode material for lithium-ion batteries, *Energy Fuels* 36 (2022) 12261–12270, <https://doi.org/10.1021/acs.energyfuels.2c01805>.
- [37] A. Van Bomme, J.R. Dahn, Analysis of the growth mechanism of coprecipitated spherical and dense nickel, manganese, and cobalt-containing hydroxides in the presence of aqueous ammonia, *Chem. Mater.* 21 (2009) 1500–1503, <https://doi.org/10.1021/cm803144d>.
- [38] T. Song, Q. Zhang, Y. Chen, P. Zhu, E. Kendrick, Synthesis and design of NaNi_{1/3}Fe_{1/3}Mn_{1/3}O₂ cathode materials for long-life sodium-ion batteries, *Chem. Eng. J. Adv.* 16 (2023), <https://doi.org/10.1016/j.cej.2023.100572>.
- [39] A. Langella, A. Massaro, A.B. Muñoz-García, M. Pavone, Atomistic insights into solid-state phase transition mechanisms of P2-Type layered Mn oxides for high-energy Na-Ion battery cathodes, *ACS Energy Lett.* 10 (2025) 1089–1098, <https://doi.org/10.1021/acscenergylett.4c03335>.
- [40] A. Massaro, G. Lingua, F. Bozza, A. Piovano, P.P. Prossini, A.B. Muñoz-García, M. Pavone, C. Gerbaldi, P2-Type Na_{0.84}Li_{0.1}Ni_{0.27}Mn_{0.63}O₂-Layered oxide Na-Ion battery cathode: structural insights and electrochemical compatibility with room-temperature ionic liquids, *Chem. Mater.* 36 (2024) 7046–7055, <https://doi.org/10.1021/acs.chemmater.4c01311>.
- [41] A. Langella, A. Massaro, A.B. Muñoz-García, M. Pavone, First-principles insights on solid-state phase transitions in P2-NaxMnO₂-Based high energy cathode during Na-Ion battery operations, *Chem. Mater.* 36 (2024) 2370–2379, <https://doi.org/10.1021/acs.chemmater.3c02981>.
- [42] A. Massaro, F. Fasulo, A. Pecoraro, A. Langella, A.B. Muñoz-García, M. Pavone, First-principles design of nanostructured electrode materials for Na-ion batteries: challenges and perspectives, *Phys. Chem. Chem. Phys.* 25 (2023) 18623–18641, <https://doi.org/10.1039/d3cp01201h>.
- [43] A. Zunger, S.H. Wei, L.G. Ferreira, J.E. Bernard, Special quasirandom structures, *Phys. Rev. Lett.* 65 (3) (1990) 353, <https://doi.org/10.1103/PhysRevLett.65.353>.
- [44] D. Gehringer, M. Friák, D. Holec, Models of configurationally-complex alloys made simple, *Comput. Phys. Commun.* 286 (2023) 108664, <https://doi.org/10.1016/j.cpc.2023.108664>.
- [45] J.P. Perdew, K. Burke, M. Ernzerhof, Generalized gradient approximation made simple, *Phys. Rev. Lett.* 77 (18) (1996) 3865, <https://doi.org/10.1103/PhysRevLett.77.3865>.
- [46] A. Massaro, F. Fasulo, A. Pecoraro, A. Langella, A.B. Muñoz-García, M. Pavone, First-principles design of nanostructured electrode materials for Na-ion batteries: challenges and perspectives, *Phys. Chem. Chem. Phys.* 25 (2023) 18623–18641, <https://doi.org/10.1039/d3cp01201h>.
- [47] A. Langella, A. Massaro, A.B. Muñoz-García, M. Pavone, Atomistic insights into solid-state phase transition mechanisms of P2-Type layered Mn oxides for high-energy Na-Ion battery cathodes, *ACS Energy Lett.* (2025) 1089–1098, <https://doi.org/10.1021/acscenergylett.4c03335>.
- [48] S. Grimme, J. Antony, S. Ehrlich, H. Krieg, A consistent and accurate ab initio parametrization of density functional dispersion correction (DFT-D) for the 94 elements H-Pu, *J. Chem. Phys.* 132 (2010), <https://doi.org/10.1063/1.3382344>.
- [49] G. Kresse, J. Furthmüller, Efficient iterative schemes for ab initio total-energy calculations using a plane-wave basis set, *Phys. Rev. B* 54 (16) (1996) 11169, <https://doi.org/10.1103/PhysRevB.54.11169>.
- [50] P.E. Blöchl, Projector augmented-wave method, *Phys. Rev. B* 50 (24) (1994) 17953, <https://doi.org/10.1103/PhysRevB.50.17953>.
- [51] G. Kresse, D. Joubert, From ultrasoft pseudopotentials to the projector augmented-wave method, *Physical review b* 59 (3) (1999) 1758, <https://doi.org/10.1103/PhysRevB.59.1758>.
- [52] V. Blum, R. Gehrke, F. Hanke, P. Havu, V. Havu, X. Ren, K. Reuter, M. Scheffler, Ab initio molecular simulations with numeric atom-centered orbitals, *Comput. Phys. Commun.* 180 (2009) 2175–2196, <https://doi.org/10.1016/j.cpc.2009.06.022>.
- [53] J. Heyd, G.E. Scuseria, M. Ernzerhof, Erratum: hybrid functionals based on a screened coulomb potential, *J. Chem. Phys.* 118 (2003) 8207, <https://doi.org/10.1063/1.2204597>. *Journal of Chemical Physics* 124 (2006).
- [54] J. Heyd, G.E. Scuseria, M. Ernzerhof, Hybrid functionals based on a screened Coulomb potential, *J. Chem. Phys.* 118 (2003) 8207–8215, <https://doi.org/10.1063/1.1564060>.
- [55] A. Tkatchenko, R.A. Distasio, R. Car, M. Scheffler, Accurate and efficient method for many-body van der Waals interactions, *Phys. Rev. Lett.* 108 (2012), <https://doi.org/10.1103/PhysRevLett.108.236402>.
- [56] C. Delmas, C. Fouassier, P. Hagenmuller, Structural classification and properties of the layered oxides, *Physica B+C* 99 (1–4) (1980) 81–85, [https://doi.org/10.1016/0378-4363\(80\)90214-4](https://doi.org/10.1016/0378-4363(80)90214-4).
- [57] B. Mortemard De Boisse, J.H. Cheng, D. Carlier, M. Guignard, C.J. Pan, S. Bordère, D. Filimonov, C. Drathen, E. Suard, B.J. Hwang, A. Wattiaux, C. Delmas, O3-

- NaxMn1/3Fe2/3O2 as a positive electrode material for Na-ion batteries: structural evolutions and redox mechanisms upon Na⁺ (de)intercalation, *J. Mater. Chem. A Mater.* 3 (2015) 10976–10989, <https://doi.org/10.1039/c4ta06688j>.
- [58] Y. You, A. Dolocan, W. Li, A. Manthiram, Understanding the air-exposure degradation chemistry at a nanoscale of layered oxide cathodes for sodium-ion batteries, *Nano Lett.* 19 (2019) 182–188, <https://doi.org/10.1021/acs.nanolett.8b03637>.
- [59] Y.Y. Wang, X. Song, S. Liu, G.R. Li, S.H. Ye, X.P. Gao, Elucidating the effect of the dopant ionic radius on the structure and electrochemical performance of Ni-Rich layered oxides for lithium-ion batteries, *ACS Appl. Mater. Interfaces* 13 (2021) 56233–56241, <https://doi.org/10.1021/acsami.1c17991>.
- [60] S. Feng, C. Zheng, Z. Song, X. Wu, M. Wu, F. Xu, Z. Wen, Boosting fast ionic transport and stability of O3-NaNi1/3Fe1/3Mn1/3O2 cathode via Al/Cu synergistically modulating microstructure for high-rate sodium-ion batteries, *Chem. Eng. J.* 475 (2023), <https://doi.org/10.1016/j.cej.2023.146090>.
- [61] S. Gao, Z. Zhu, H. Fang, K. Feng, J. Zhong, M. Hou, Y. Guo, F. Li, W. Zhang, Z. Ma, F. Li, Regulation of coordination chemistry for ultrastable layered oxide cathode materials of sodium-ion batteries, *Adv. Mater.* 36 (2024), <https://doi.org/10.1002/adma.202311523>.
- [62] H. Yang, Q. Zhang, M. Chen, Y. Yang, J. Zhao, Unveiling the origin of air stability in polyanion and layered-oxide cathode materials for sodium-ion batteries and their practical application considerations, *Adv. Funct. Mater.* 34 (2024), <https://doi.org/10.1002/adfm.202308257>.
- [63] M. Yan, Z.A. Jin, P. Wang, Y. Guo, Y.X. Yin, S. Xu, In situ surface engineering O3-layered oxide cathode via Na3PO4/P3-layered oxide dual coating layers, *Electrochim. Acta* 521 (2025), <https://doi.org/10.1016/j.electacta.2025.145911>.
- [64] C. Jiang, Y. Wang, Y. Xin, Q. Zhou, Y. Pang, B. Chen, Z. Wang, H. Gao, A high-rate and air-stable cathode material for sodium-ion batteries: yttrium-substituted O3-type Ni/Fe/Mn-based layered oxides, *J. Mater. Chem. A Mater.* 12 (2024) 13915–13924, <https://doi.org/10.1039/d4ta01852d>.
- [65] X. Zhang, H. Chen, S. Xu, M. Zhou, R. Nie, Y. Yang, C. Li, H. Zhou, Zinc-substituted P2-type Na0.67Ni0.23Zn0.1Mn0.67O2 cathode with improved rate capability and cyclic stability for sodium-ion storage at high voltage, *J. Alloys Compd.* 968 (2023), <https://doi.org/10.1016/j.jallcom.2023.172190>.
- [66] Y.Y. Ting, P.M. Kowalski, Refined DFT+U method for computation of layered oxide cathode materials, *Electrochim. Acta* 443 (2023), <https://doi.org/10.1016/j.electacta.2023.141912>.
- [67] D.A. Aksyonov, S.S. Fedotov, K.J. Stevenson, A. Zhugayevych, Understanding migration barriers for monovalent ion insertion in transition metal oxide and phosphate based cathode materials: a DFT study, *Comput. Mater. Sci.* 154 (2018) 449–458, <https://doi.org/10.1016/j.commatsci.2018.07.057>.
- [68] A. Massaro, A. Langella, A.B. Muñoz-García, M. Pavone, First-principles insights on anion redox activity in NaxFe1/8Ni1/8Mn3/4O2: toward efficient high-energy cathodes for Na-ion batteries, *J. Am. Ceram. Soc.* 106 (2023) 109–119, <https://doi.org/10.1111/jace.18494>.
- [69] A. Massaro, A.B. Muñoz-García, P.P. Proisini, C. Gerbaldi, M. Pavone, Unveiling oxygen redox activity in P2-Type NaxNi0.25Mn0.68O2High-Energy cathode for Na-Ion batteries, *ACS Energy Lett.* 6 (2021) 2470–2480, <https://doi.org/10.1021/acseenergylett.1c01020>.
- [70] A. Massaro, A. Langella, C. Gerbaldi, G.A. Elia, A.B. Muñoz-García, M. Pavone, Ru-Doping of P2-NaxMn0.75Ni0.25O2-Layered oxides for high-energy Na-Ion battery cathodes: first-principles insights on activation and control of reversible oxide redox chemistry, *ACS Appl. Energy Mater.* 5 (2022) 10721–10730, <https://doi.org/10.1021/acsaem.2c01455>.
- [71] A. Massaro, A. Langella, A.B. Muñoz-García, M. Pavone, First-principles insights on anion redox activity in NaxFe1/8Ni1/8Mn3/4O2: toward efficient high-energy cathodes for Na-ion batteries, *J. Am. Ceram. Soc.* 106 (2023) 109–119, <https://doi.org/10.1111/jace.18494>.
- [72] A. Massaro, A.B. Muñoz-García, P.P. Proisini, C. Gerbaldi, M. Pavone, Unveiling oxygen redox activity in P2-Type NaxNi0.25Mn0.68O2High-Energy cathode for Na-Ion batteries, *ACS Energy Lett.* 6 (2021) 2470–2480, <https://doi.org/10.1021/acseenergylett.1c01020>.
- [73] M. Yan, Z.A. Jin, P. Wang, Y. Guo, Y.X. Yin, S. Xu, In situ surface engineering O3-layered oxide cathode via Na3PO4/P3-layered oxide dual coating layers, *Electrochim. Acta* 521 (2025), <https://doi.org/10.1016/j.electacta.2025.145911>.
- [74] K. Xue, S. Yang, F. Lai, X. Zhang, Y. Xie, G. Yang, K. Pan, Q. Li, H. Wang, Synergistic effect of anchoring transitional/interstitial sites on boosting structural and electrochemical stability of O3-Type layered sodium oxides, *ACS Appl. Mater. Interfaces* 17 (2025) 1286–1294, <https://doi.org/10.1021/acsaami.4c17755>.
- [75] W. Wang, Y. Sun, P. Wen, Y. Zhou, D. Zhang, Enhanced conduction and phase transition reversibility of O3-type NaNi1/3Fe1/3Mn1/3O2 cathode via Ta doping for high-performance sodium-ion battery, *J. Energy Storage* 79 (2024), <https://doi.org/10.1016/j.est.2023.110177>.
- [76] Y. Gao, G. Zhang, Y. Ji, Z. Yang, Y. Fan, X. Shi, Y. Huang, Tailoring the electronic structure of O3-type layered oxide cathodes to achieve long-cycle life and high-rate performance sodium-ion batteries, *J. Mater. Chem. A Mater.* 13 (2024) 3106–3114, <https://doi.org/10.1039/d4ta06988a>.
- [77] M. Islam, M. Akbar, D. Han, B. Ali, Y. Jeong Choi, J. Lee, G. Choi, J.H. Park, J. Y. Kim, H.G. Jung, K. Yoon Chung, D. Kim, Y.M. Kang, K.W. Nam, Unraveling vacancy-induced oxygen redox reaction and structural stability in Na-based layered oxides, *Chem. Eng. J.* 431 (2022), <https://doi.org/10.1016/j.cej.2021.133962>.
- [78] J.Y. Hwang, S.T. Myung, D. Aurbach, Y.K. Sun, Effect of nickel and iron on structural and electrochemical properties of O3 type layer cathode materials for sodium-ion batteries, *J. Power Sources* 324 (2016) 106–112, <https://doi.org/10.1016/j.jpowsour.2016.05.064>.
- [79] J. Yue, F. Xiong, Z. Shadike, X. Gao, J. Chen, L. Pi, Y. Yuan, B. Qu, P. Adamson, L. Ma, Q. Li, P.G. Bruce, A layer-structured high entropy oxide with highly reversible Fe3+/Fe4+ redox as advanced cathode material for sodium ion batteries, *J. Power Sources* 627 (2025), <https://doi.org/10.1016/j.jpowsour.2024.235735>.
- [80] Y. Cai, Z. Luo, K. Liao, X. Xin, M. Zhou, Y.J. Cheng, R. Liu, X. Yan, S. Papović, K. Zheng, K. Świerczek, Dual-site Zn doping boosts longevity and air stability of O3-type NaNi1/3Fe1/3Mn1/3O2 cathode for high-performance sodium-ion batteries, *J. Power Sources* 631 (2025), <https://doi.org/10.1016/j.jpowsour.2025.236272>.
- [81] H. Zhao, J. Li, W. Liu, H. Xu, X. Gao, J. Shi, K. Yu, X. Ding, Integrated titanium-substituted air stable O3 sodium layered oxide electrode via a complexant assisted route for high capacity sodium-ion battery, *Electrochim. Acta* 388 (2021), <https://doi.org/10.1016/j.electacta.2021.138561>.
- [82] K. Kubota, N. Fujitani, Y. Yoda, K. Kuroki, Y. Tokita, S. Komaba, Impact of Mg and Ti doping in O3 type NaNi1/2Mn1/2O2on reversibility and phase transition during electrochemical Na intercalation, *J. Mater. Chem. A Mater.* 9 (2021) 12830–12844, <https://doi.org/10.1039/d1ta01164b>.
- [83] F. Ding, C. Zhao, D. Zhou, Q. Meng, D. Xiao, Q. Zhang, Y. Niu, Y. Li, X. Rong, Y. Lu, L. Chen, Y.S. Hu, A novel Ni-rich O3-Na[Ni0.60Fe0.25Mn0.15]O2 cathode for Na-ion batteries, *Energy Storage Mater.* 30 (2020) 420–430, <https://doi.org/10.1016/j.jensm.2020.05.013>.